Journal of
Ceramic Science
and Technology

J. Ceram. Sci. Tech., 07 [02] 145-154 (2016)
DOI: 10.4416/JCST2016-00012
available online at: http://www.ceramic-science.com

Microscale-Motivated Continuum Damage Simulations of Brittle Ceramics under Thermomechanical Loading

J. Gundlach*[1], D. Henneberg[1], J. Scheel[1], A. Ricoeur[1]

[1]University of Kassel, Institute of Mechanics, Chair of Engineering Mechanics/
Continuum Mechanics, Mönchebergstraße 7, D-34119 Kassel, Germany

received February 1, 2016; received in revised form March 20, 2016; accepted May 2, 2016

Abstract

Two approaches towards modeling damage in a brittle material caused by thermomechanical loading are presented. Both rely on microcrack growth, in the first case in a homogeneous matrix, in the second one at grain boundaries. Two-scale simulations e.g. of thermal shocks applied to single-phase or layered structures are performed in connection with the finite element method. Damage and crack patterns are predicted just as quantities like residual strength or critical temperature jumps.

Keywords: Thermal shock, damage simulations, multiscale models, effective material properties

I. Introduction

Being brittle by nature, ceramics can withstand large compressive stresses. As soon as they are exposed to tensile stress, however, failure is observed with comparatively small loads. This aspect is usually taken into account in the design of mechanically loaded structures made of ceramic materials. Thermal loading, on the other hand, induces residual stresses, being both compressive and tensile in order to satisfy the global mechanical equilibrium. Particularly thermal shock in terms of fast and intense surface heating or cooling is a source of large local stress, where predominantly tensile contributions lead to cracking and local failure. In many cases the rupture is not even visible, the damaged zone being underneath the surface at the point of maximum stress. Further loading may then lead to a sudden unexpected fracture of the whole structure.

On the microscale, small cracks are predominantly responsible for the onset and growth of damaged zones. Typically, lengths of relevant microcracks are in a range of a few to some tens of microns, thus having the same order of magnitude as the average grain size of a polycrystalline ceramic. Crack growth can be trans- or intergranular, in principle, and exhibit interactions with the microstructure. It is observed at any intensity of loading, being denoted undercritical if the crack tip loading is below the material-inherent crack resistance or fracture toughness, respectively. Corrosive media play an important role in the undercritical crack growth regime, being responsible for a gradual degradation and fatigue of the ceramic structure [1,2].

As thermal shock is in the focus of interest, undercritical microcrack growth is not relevant, however. Induced residual stresses are usually large enough to provide enough energy for critical crack growth, where the crack tip loading equals the fracture toughness of the material. The latter is supposed to increase during an early stage of crack growth due to interactions with the microstructure, thus providing the possibility of stable crack extension. Just a few thermal shock cycles are commonly sufficient to induce severe local damage and to nucleate a macroscopic crack.

In this paper, models are presented describing the process of microcrack initiation and growth within a continuum mechanical framework. In contrast to fracture mechanical approaches, where a crack is introduced as a pair of free surfaces, microcrack growth is described by an internal state variable, representing the accumulated crack surfaces related to the edge lengths of representative volume elements (RVE). The evolution of this internal or damage variable is governed by fracture mechanical relations of crack length and local stress. The influence of the cracks on macroscopic properties, e.g. the elastic constants, is taken into account by means of homogenization of the defect phase in the RVE, thus bridging the two scales.

Two different models are employed on the microscale, an analytical one accounting for cracks in a homogeneous matrix, and a numerical one where grain boundaries and their delamination are considered. The finite element method is applied to solve thermomechanical boundary value problems. The theoretical background is briefly outlined, partly referring to previously published work [3,4]. The focus of this paper is on the illustration of the potential of the numerical methods in investigating the degradation of e.g. refractory ceramics under thermomechanical loading. A variety of results from numerical simulation is thus presented, ranging from the growth of macroscopic cracks to typical applications of single-phase and layered refractory structures.

* Corresponding author: gundlach@uni-kassel.de

II. Two-Scale Modeling and Implementation

The results presented in this work have been generated using a continuum damage approach for brittle materials [3–5]. For this purpose, so-called cell models are employed, incorporating either microcracks or cohesive grain boundaries on a microscopic level. The overall concepts of the solution procedures are illustrated in the subsequent sections.

In general, the solution is sought for the thermomechanical initial boundary value problem, on the macroscopic scale with coordinates x_i^m (cf. Fig. 1) governed by

$$\sigma_{ij,j} = 0, \tag{1}$$

$$\varrho c\dot{\theta} = \lambda\, \theta_{,ii}, \tag{2}$$

with prescribed temperatures $\bar{\theta}$, displacements $\bar{u}_i$, stresses $\bar{t}_i$ and heat fluxes $\bar{q}_i$ as suitable boundary conditions. In Eq. (1) volume forces and inertia terms are neglected, as are material anisotropies and gradations of local properties in Eq. (2). Furthermore, the analytical notation is applied introducing indices for tensor coordinates, implying summation over double indices, and using the comma convention for partial derivatives. The parameters of the energy balance in Eq. (2), i.e. mass density ϱ, specific heat capacity c, and thermal conductivity λ, are allowed to be temperature-dependent. The stresses σ_{ij} and temperatures in equations (1) and (2) are quantities valid on the macroscopic level of the two-scale concept displayed in Fig. 1. The microscopic level is defined by an RVE, size d^3, which is intended to describe the properties of the particular microstructure and is associated with a point P at a macroscopic coordinate x_i^m. On the one hand, an RVE is claimed to be sufficiently small in order to allow this punctual allocation, on the other hand, it must be large compared to the dimensions of the microstructural features: $l \ll d \ll L$. For ceramics, an appropriate choice is $d \approx 0.1$ mm [6]. The heterogeneities taken into account in this study are either microcracks of arbitrary orientation or grain boundaries in a polycrystal. Owing to these discontinuities, both stresses and strains are field variables, depending on the microscopic scale x_i. In the process of homogenization, these fields are averaged within the respective volume V of the RVE, to define the mechanical state at each macroscopic point:

$$\langle\sigma_{ij}\rangle = \frac{1}{V}\int_V \sigma_{ij}(x_k)\,\mathrm{d}V, \quad \langle\varepsilon_{ij}\rangle = \frac{1}{V}\int_V \varepsilon_{ij}(x_k)\,\mathrm{d}V, \tag{3}$$

where the brackets $\langle\cdot\rangle$ indicate volume-averaged quantities henceforth. A constitutive law in this thermomechanical framework relates these macroscopic values according to Hooke's law including thermal expansion:

$$\langle\sigma_{ij}\rangle = C^*_{ijkl}(\langle\varepsilon_{kl}\rangle - \alpha\delta_{kl}\theta_{nn}). \tag{4}$$

Again, the expansion coefficient α varies with temperature and is assumed to be isotropic. The identity tensor is denoted as δ_{kl}. Note that none of the thermal parameters is affected by the existence or growth of microcracks. In contrast to metals, the thermal conductivity of ceramics is not sufficiently high to deflect the heat flux around existing cracks. The lines of thermal flux rather penetrate the crack slit unperturbed, the latter being very thin due to the low crack resistance of the material. This behavior which has been illustrated in numerical experiments [7] does not depend on emerging displacement jumps until fracture. Consequently, all crack-like heterogeneities are considered as thermally permeable. Hence, the heat equation is fully decoupled from the momentum equation and the effective stiffness tensor C^*_{ijkl} represents the impact of potential damage evolution solely. In the following, the used cell models describing the effective constants and their dependence on internal variables are explained.

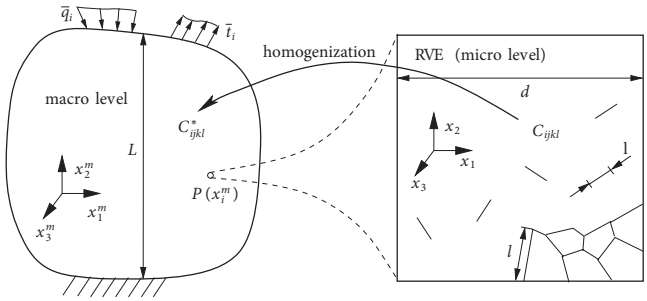

Fig. 1: Concept of homogenization within the thermomechanical two-scale problem with boundary heat fluxes $\bar{q}_i$ and tractions $\bar{t}_i$. Spatially varying elastic constants C_{ijkl} are replaced by effective constants C^*_{ijkl} for the whole RVE.

(1) Analytical cell model of microcrack growth

A more detailed motivation for this approach, based on microcrack initiation and growth, has been introduced in previous efforts [3]. With the divergence theorem and the mechanical equilibrium according to Eq. (1), macroscopic stress can be rewritten as the surface integral

$$\langle\sigma_{ij}\rangle = \frac{1}{V}\int_A t_i x_j\,\mathrm{d}A, \tag{5}$$

while the strain on macroscopic scale yields

$$\langle\varepsilon_{ij}\rangle = \frac{1}{2V}\int_A (u_i n_j + u_j n_i)\,\mathrm{d}A, \tag{6}$$

assuming small deformations. With regard to the void of a crack and the surrounding material as discrete phases with segregated stresses, strains, and material properties, equation (6) can be reorganized (cf. [8]) to

$$\langle\varepsilon_{ij}\rangle = \langle\varepsilon_{ij}\rangle_M + \frac{1}{2V}\int_{A_C} (\Delta u_i n_j + \Delta u_j n_i)\,\mathrm{d}A = \langle\varepsilon_{ij}\rangle_M + \langle\varepsilon_{ij}\rangle_C. \tag{7}$$

In this expression, the subscripts M and C denote averaged strains valid for the matrix phase and the crack phase A_C, respectively. In contrast to the macroscopic strains, the stresses consist only of those coming from the matrix phase: $\langle\sigma_{ij}\rangle = \langle\sigma_{ij}\rangle_M$. Whereas the matrix deformations $\langle\varepsilon_{ij}\rangle_M$ and stresses $\langle\sigma_{ij}\rangle$ can be easily connected by a linear elastic law, the strains of the defect phase $\langle\varepsilon_{ij}\rangle_C$ require the integration of displacement jumps attributed to cracks. They must be evaluated along the crack faces for certain stress states. For this purpose, the following assumptions are made:

i) The distribution of microcracks is considered as dilute, such that the impact of the interaction among existing cracks on strains and stresses is not included.

ii) The stresses along the boundary of each RVE are prescribed with a uniform value according to a Reuss approximation.
iii) All solutions are obtained in a hypothesized state of plane stress.

With these preconventions, the displacement jumps are determined with the Griffith crack solution

$$\Delta u_i(x_i) = \frac{4\langle\sigma_{i2}\rangle}{E}\sqrt{a^2 - x_1^2}, \quad (i = 1,2) \tag{8}$$

with E denoting Young's modulus of the matrix phase and a the half crack length. Now, the integration in Eq. (7) is feasible and the macroscopic strains of the crack phase can be expressed by means of the macroscopic stresses. In total, the elasticity law can be formulated with compliance contributions coming from the matrix and the defect phase:

$$\begin{bmatrix} \langle\varepsilon_{11}\rangle \\ \langle\varepsilon_{22}\rangle \\ 2\langle\varepsilon_{12}\rangle \end{bmatrix} = \frac{1}{E}\begin{bmatrix} 1 & -\nu & 0 \\ -\nu & 1+\frac{f\pi}{2} & 0 \\ 0 & 0 & 2(1+\nu)+\frac{f\pi}{2} \end{bmatrix}\begin{bmatrix} \langle\sigma_{11}\rangle \\ \langle\sigma_{22}\rangle \\ \langle\sigma_{12}\rangle \end{bmatrix} \tag{9}$$

The above relations are functions of $f = \frac{4a^2}{d^2}$, an internal variable representing the square of the length of the microcrack in respect of the edge of the RVE. This parameter is interpreted as crack density and used to quantify the local damage. If f reaches unity, a crack has proceeded through the entire volume element. In that case, the material is totally damaged at that specific location.

The material law displayed in Eq. (9) is anisotropic due to the additional compliance in the $\langle\varepsilon_{22}\rangle$ - component perpendicular to the crack ligament. For that reason, it is not well-suited as starting point of an isotropic material, where tiny microcracks of equivalent lengths are distributed with arbitrary orientation. An appropriate behaviour is derived, considering a generic crack rotated by the angle α with respect to the x_i-coordinates, as shown in Fig. 2. Similar to the linear splitting of deformations in Eq. (7), it is possible to divide the effective compliance tensor in two parts:

$$C^{*,\alpha}_{ijkl} = \left[C^{-1}_{ijkl_M} + C^{-1,\alpha}_{ijkl_C}\right]^{-1}. \tag{10}$$

The effective constants of the matrix phase are not affected by any rotation inasmuch as Hooke's law is isotropic. From Eq. (9) it is known that

$$\begin{aligned} C^{-1,\alpha}_{2222_C} &= \frac{f\pi}{2E}, \\ C^{-1,\alpha}_{1212_C} &= C^{-1,\alpha}_{2121_C} = C^{-1,\alpha}_{1221_C} = C^{-1,\alpha}_{2112_C} = \frac{f\pi}{8E}, \end{aligned} \tag{11}$$

with all other components being zero. For the arbitrary-oriented crack, these values are only valid in the rotated coordinate system x_i^{α}, however. To obtain $C^{-1}_{ijkl_C}$ such that cracks are oriented randomly, the entries must be transformed to the x_i-coordinates and integrated over any possible orientation α (cf. [9]):

$$C^{-1}_{ijkl_C} = \frac{1}{2\pi}\int_0^{2\pi} Q_{ip}Q_{jq}Q_{kr}Q_{ls}C^{-1,\alpha}_{pqrs_C}\,\mathrm{d}\alpha \tag{12}$$

In this algorithm, Q_{ij} is an orthogonal tensor, transferring the components. If this is applied to the results in Eq. (11), the outcome is an isotropic relation reflecting the impact of the initial microcrack distribution:

$$\begin{bmatrix} \langle\varepsilon_{11}\rangle \\ \langle\varepsilon_{22}\rangle \\ 2\langle\varepsilon_{12}\rangle \end{bmatrix} = \frac{1}{E}\begin{bmatrix} 1+\frac{f_0\pi}{4} & -\nu & 0 \\ -\nu & 1+\frac{f_0\pi}{4} & 0 \\ 0 & 0 & 2(1+\nu)+\frac{f_0\pi}{2} \end{bmatrix}\begin{bmatrix} \langle\sigma_{11}\rangle \\ \langle\sigma_{22}\rangle \\ \langle\sigma_{12}\rangle \end{bmatrix} \tag{13}$$

with

$$\begin{aligned} C^{-1}_{1111_C} &= C^{-1}_{2222_C} = \frac{f_0\pi}{4E}, \\ C^{-1}_{1212_C} &= C^{-1}_{2121_C} = C^{-1}_{1221_C} = C^{-1}_{2112_C} = \frac{f_0\pi}{8E}. \end{aligned} \tag{14}$$

The above-outlined material law is the starting point of every simulation with the initial damage of $f_0 = \frac{4a_0^2}{d^2} \ll 1$, a_0 being the initial microcrack length. Yet, isotropy within an RVE is lost as soon as it comes to loads of a critical magnitude, initiating the propagation of microcracks which are oriented perpendicular to local maximum principal stresses. Then, only these cracks are considered as crucial source of failure since they will grow in the first place. Accordingly, the anisotropic law described in Eq. (9) is used henceforward. In that case, the effective constants are transformed to the macroscopic coordinates x_i^m by the appropriate rotation law depending on the particular crack orientation.

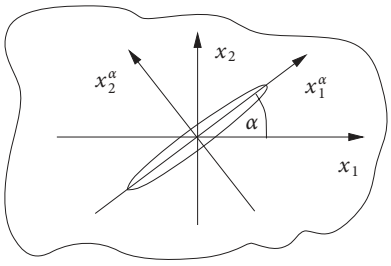

Fig. 2: Arbitrarily oriented crack with reference coordinate system x_i and rotated coordinate system x_i^{α}.

The criterion of microcrack evolution corresponds to an R-curve-based Mode-I macrocrack law [10]. Thus, it comes to the extension of a microcrack in an RVE if

$$K_I(\sigma, \alpha) > K_R(\Delta\alpha), \tag{15}$$

where K_I results from the largest positive principal stress value of the macroscopic scale according to

$$K_I = \langle\sigma_I\rangle\sqrt{\pi\alpha}, \tag{16}$$

and K_R is evaluated from a function of the type

$$K_R = K_\infty\left(1 - \left(1 - \frac{K_0}{K_\infty}\right)e^{-\eta\frac{\Delta\alpha}{\alpha_0}}\right). \tag{17}$$

In the R-curve equation, K_0 and K_∞ denote the initial and plateau values, respectively, $\Delta\alpha = \alpha - \alpha_0$ the crack propagation length, and η determines the gradient of the crack resistance. From Eqs. (15) and (16) and the definition of the damage parameter f, the evolution equation of the internal variable is obtained in a compact form as

$$\mathrm{d}f = H\left(\frac{\langle\sigma_I\rangle(d\pi)^{\frac{1}{2}}f^{\frac{1}{4}}}{\sqrt{2}K_R(f,f_0)} - 1\right)\mathrm{d}\hat{f}; \quad \mathrm{d}\hat{f} = \text{const}, \tag{18}$$

where H is the Heaviside step function and $\mathrm{d}\hat{f}$ is a small damage increment caused by crack growth. The stability of a potential crack growth is provided whilst

$$\frac{dK_I}{df} > \frac{dK_R}{df}. \tag{19}$$

The outlined procedure is applied at every integration point of the macroscopic finite element model. Once the critical value $f = 1$ is reached, the effective stiffness is instantly reduced to a small but finite value, to accommodate the event of rupture. Stresses are reduced, likewise attributed to the local softening of the material.

The presumption of an increasing cracking resistance with regard to defect extension as described in Eq. (17) is one way to obtain stable microcrack growth and thus values $0 < f < 1$. According to Eqs. (18) and (19), stable crack growth is also possible if $\langle \sigma_I \rangle$ is reduced with constant K_R due to the reduction of local stiffness C^*_{ijkl} associated with the damage progress df. If there is no stable crack growth, the model still works, however, the calculation of effective anisotropic compliances will be omitted in that case.

(2) Two-scale FE model applying numerical homogenization

In contrast to the analytical cell model, the displacements and strains, respectively, are used to formulate the boundary conditions to be imposed on the RVE, taking into account intercrystalline microcrack growth. Thus, the macro strains $\langle \varepsilon_{ij} \rangle$ are transformed onto the cell model boundary associated with the relation between strain and displacement as

$$\left.\begin{aligned} \varepsilon_{11} x_1 &= u_1 \\ \varepsilon_{22} x_2 &= u_2 \\ 2\varepsilon_{12} &= \frac{u_2}{x_1} + \frac{u_1}{x_2} \end{aligned}\right\} \; 0 \geq x_1, x_2 \geq d, \tag{20}$$

in which u_i is the displacement within the RVE where $x_1 = d$ and $x_2 = d$ provide values at the boundaries. Hill's condition postulating the equality of average and local strain energy densities [11] is satisfied by these conditions. After the boundary value problem of the cell model has been solved, the macroscopic stress tensor $\langle \sigma_{ij} \rangle$ and effective tangent moduli C^*_{ijkl} are obtained. Again, one very important requirement of the scales separation is that the length scale of the global macroscopic model L is much larger than the dimension of the RVE d. The main ideas of related homogenization methods have been established in [12–14] There are similar approaches, e.g. the multi-scale projection method [15] or the FE^2-method [16], typically applied to nonlinear problems with periodic boundary conditions at large deformations. Trends and challenges of the multi-scale homogenization methods are given in [17].

Fig. 3 depicts an example of such randomly distributed grains in a domain with outer unit normals n_i. The dimensions of the RVE are d for the height and the length as well. In brittle materials, cracks often are initiated and propagate along the interfaces between the crystallites known as grain boundaries (intercrystalline crack growth) [18]. The RVEs with randomly distributed grains are created automatically based on parametric preprocessing. In contrast to the previously presented model of crack distributions in a homogeneous matrix (cf. section II(1)), they establish the influence of the grain size in the simulations by introducing that quantity as scale parameter in the cohesive law.

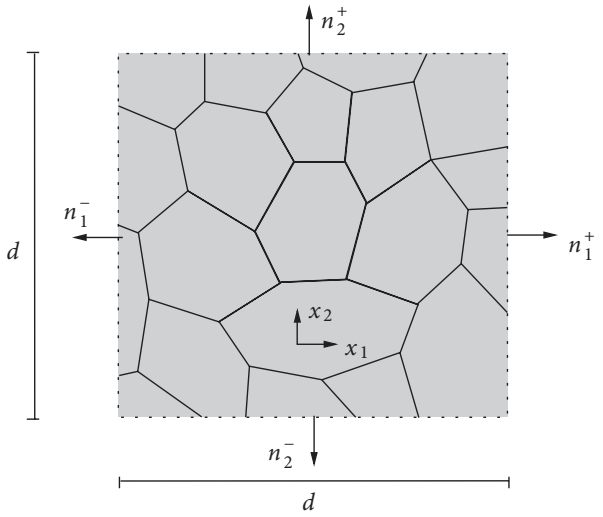

Fig. 3: Representative volume element (cell model) representing a polycrystalline material with unit normal vectors n_i.

For the sake of simplicity, the separation process is assumed to be based on bi-linear relationships between interfacial traction and separation displacement. Different constitutive laws have been used in cohesive zone models e.g. in Barenblatt's atomic force attraction law [19], in Dugdale's model frequently used for computational fracture research in ductile materials [20], in Needleman's cubic model [21], or Hillerborg's bi-linear model [22].

In Fig. 4 the bi-linear cohesive zone law is displayed which is used for the RVE modeling. This traction-separation law allows for computation of the relationship between the interface restraining traction σ_R and the relative grain boundary displacement δ, finally leading to an intercrystalline crack if the critical displacement δ^c is attained. With relation of the separation δ to the average grain size, the latter parameter is introduced in the simulations.

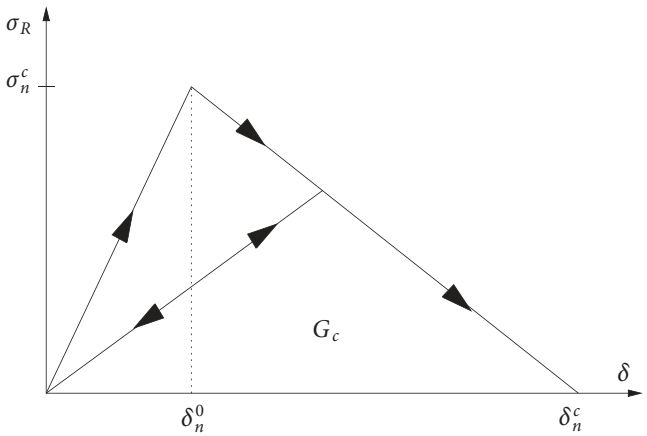

Fig. 4: Bi-linear cohesive law relating interface traction σ_R and separation displacement δ with loading and unloading paths.

Fig. 5 illustrates a grain boundary interface with all the relevant quantities. Traction vectors t_c and σ_R are related by unit normals as

$$n_c^{+/-} \cdot \sigma_R = t_c^{+/-} \tag{21}$$

The bi-linear cohesive law is described by the following equation:

$$\sigma_R = \sigma^c_{(i)} \begin{cases} \dfrac{\delta_{(i)}}{\delta^0_{(i)}}, & 0 < \delta_{(i)} < \delta^0_{(i)} \\ \dfrac{\delta^0_{(i)} - \delta_{(i)}}{\delta_{(i)} - \delta^0_{(i)}}, & \delta^0_{(i)} < \delta_{(i)} < \delta^c_{(i)} \end{cases} \tag{22}$$

with index $i = n, s$ for normal and shear separation. To avoid conflicts with the tensorial index notation, brackets $(\cdot)$ have been introduced. In the simulations, uncoupled cohesive laws are applied, i.e. the normal and tangential components of separation are not interacting. For the normal opening mode (Mode-I) there are two essential quantities, the peak value of cohesive stress σ^c_n and the related relative interfacial displacement δ^0_n. The point (σ^c_n/δ^0_n) is the onset of strain softening followed by an instable state, finally leading to crack growth at $\delta^c{}_n$. In the case of shear opening (Mode-II), the plot in Fig. 4 is qualitatively identical replacing indices n by s, where σ^c_s denotes the maximum shear stress at δ^0_s. Fig. 6 illustrates a combined normal and shear separation with relative displacements δ_n and δ_s of opposite boundaries of two grains.

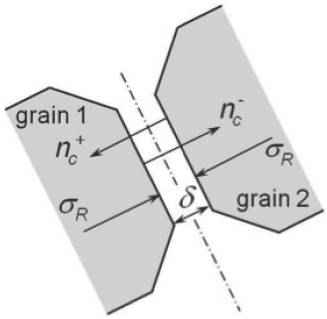

Fig. 5: Cohesive restraining stress σ_R, respective unit normal vectors $n_c^{+/-}$, and opening displacement δ between two grain boundaries at an interface with pure normal separation.

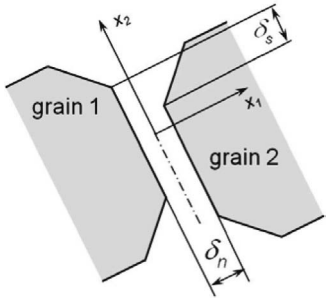

Fig. 6: Normal and shear separation δ_n, δ_s between two grains with local coordinate system x_i.

From the J-integral enclosing the cohesive zone, the following relation can be derived (cf. [23])

$$G_c = \int_0^{\delta^c} \sigma_R(\delta)\, \mathrm{d}\delta \tag{23}.$$

The area underneath the entire traction-separation curve (Fig. 4) represents the cohesive energy density or critical energy release rate G_c, i.e. the total energy per unit surface required to completely separate the interface at a given point. Integrating the bilinear function according to Eq. (22) and Fig. 4, Eq. (23) yields

$$G_c = \frac{1}{2}\sigma^c_{(i)}\delta^c_{(i)} = 2\gamma_c, \tag{24}$$

where γ_c is the specific fracture surface energy originally suggested by Griffith [24]. Including the traction vector according to Eq. (21), the cohesive law for both normal and tangential separation can be written as

$$\begin{bmatrix} t_n \\ t_s \end{bmatrix} = \begin{bmatrix} K_{nn} & K_{ns} \\ K_{sn} & K_{ss} \end{bmatrix} \begin{bmatrix} \delta_n \\ \delta_s \end{bmatrix} \tag{25}$$

where [K] is the stiffness matrix of the cohesive zone. Eq. (25) neglects the coupling of normal and shear modes, choosing $K_{ns} = K_{sn} = 0$. For the cohesive zone modeling between grains, three parameters have to be selected appropriately, i.e. the stiffnesses $K_{(i)(i)}$, the critical displacement $\delta^c_{(i)}$, and the critical energy release rate G_c.

Two stages are considered separately. Below the softening point $\delta^0_{(i)}$ the material behaves linearly. As long as this condition holds for all nodal points at any grain boundary in a local RVE, the elastic properties are represented by effective values C^*_{ijkl} which are uniquely determined, depending on the state of multiaxial stress. If degradation $(\delta > \delta^0_{(i)})$ takes place at one or more locations within an RVE, the simulation at the affected integration point of the macroscopic model is continued, coupling the two-scale FE models exchanging field quantities at each time step [4].

III. Numerical Examples and Discussion

First, results of the analytical cell model are presented. As mentioned above, the microcracks are dilutely distributed in the RVE, initially exhibiting statistical orientations leading to isotropic effective stiffness. Before structures exposed to thermal shocks are dealt with, pure mechanical loading is investigated to demonstrate the potential of the modeling approach in simulating macroscopic crack growth and crack paths.

In Fig. 7 a plate specimen is shown, being subject to tensile loading. The notch, depicted on the left-hand side of the plate fosters the initiation of microcrack growth and thus the nucleation of a macroscopic crack. In the figures, the red color indicates regions, within a numerical context representing integration points, with the damage variable being $f = 1$. Thus, the material has to be interpreted as fully ruptured at that location. Fig. 7 illustrates the evolution of the damage zone in three arbitrarily chosen frames. The damaged region, being very narrow and restricted to a small zone around the plane of symmetry, is reminiscent of a crack, being initiated at the notch and, driven by the tensile load, running straight through the plate as expected. A detail of the finite element mesh at the crack tip is shown for the right frame. Owing to the remaining but small stiffness of the damage zone at $f = 1$, an R-curve effect is obtained, leading to stable growth of short cracks, where an increasing load $\bar{\sigma}_{22}$ is required for further crack advance, whereas longer cracks exhibit instable crack growth at constant external load.

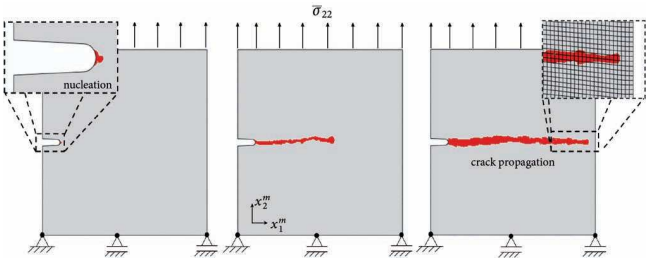

Fig. 7: Damage mechanical FE-simulation of macrocrack propagation with tensile loading σ_{22} in x_2^m-direction.

In Fig. 8 a crack path obtained from the damage model is compared to a classical fracture mechanical prediction based on free crack surfaces, an adaptive remeshing algorithm and the calculation of the J-integral [25]. The fracture mechanical numerical tool has been verified on the basis of various experiments and is intended to serve as a benchmark. A hole in the plate attracts the crack which is again exposed to tensile loading. The blue line represents the crack path from fracture mechanics, the red area is the damage zone. The crack deflection by the hole is a little overestimated with the damage mechanical approach, however, qualitatively providing the essential features of the crack path. In contrast to the fracture mechanical simulation, where an incipient crack is required in the model, the onset of a crack can likewise be predicted with damage mechanical approaches. Accordingly, crack formation at the hole is indicated by a small second damage zone in Fig. 8.

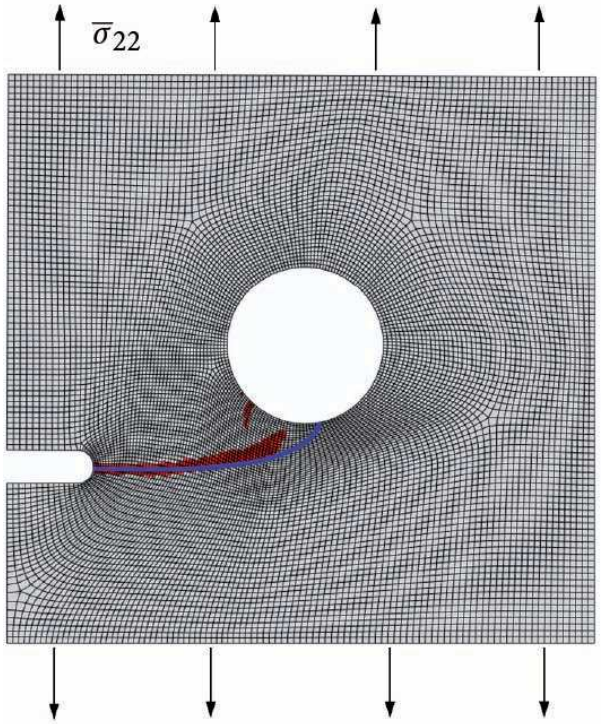

Fig. 8: Crack path in a plate with a hole predicted by a damage simulation compared to a simulation based on classical fracture mechanics.

A comparison of crack path predictions based on continuum damage mechanics and the phase field method is presented in Fig. 9. The latter calculations have been performed within the framework of another project of the joint research program [26]. A plate with nano-inclusions that are stiffer than the matrix material is exposed to tensile loading. Four arbitrarily chosen frames showing different stages of crack growth are presented. The crack is nucleated at a sharp notch, located on the left-hand side of the specimen. With a closer look at the continuum damage mechanical simulation in the left column, a further crack nucleation is predicted in the third frame, starting from the bottom of one inclusion. In general, crack path deflections are observed due to the stiffness discontinuities, yielding similar results for both modeling approaches.

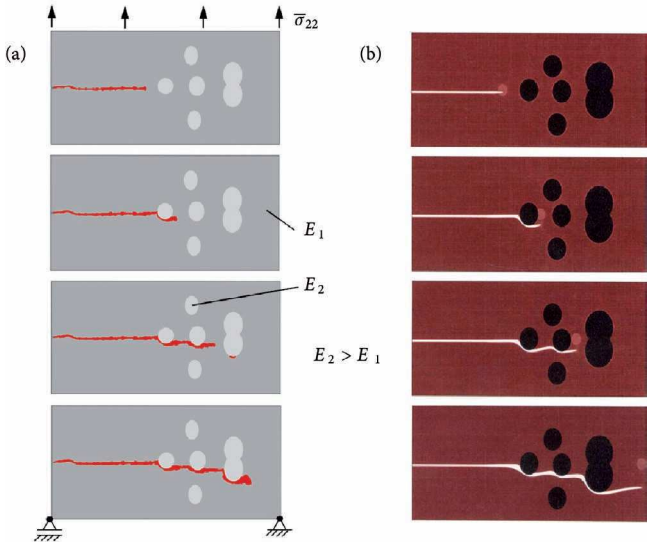

Fig. 9: Comparison of crack paths in a plate under tensile stress with spheric inclusions provided (a) by the continuum damage approach and (b) by the phase field method.

Fig. 10 illustrates results of a brittle structure with thermal shock loading at a small section of the top surface. Boundary conditions and material data of the simulations are largely based on experiments within the framework of another project of the joint research program, where disks made of AZT-refractory ceramics have been exposed to an electron beam acting on a 4 cm^2 part of the surface [27]. The absorbed power density is estimated to be as large as $\bar{q} = 42$ MW/m^2, in the experiments being maintained as long as 0.5 s (Fig. 10(a)) and 0.1 s (Fig. 10(b)), respectively. In the simulations, the remaining surface of the model is assumed to be adiabatic. Mechanically the specimen is supported at the bottom edge, allowing for free extension due to the heating. The thermal loading is intermittent, exhibiting constant power densities, interrupted by two seconds of rest.

The plots in Fig. 10 show three stages of damage after different numbers of load cycles, from 5 to 50. The blue regions are those of partial damage, where $f_0 < f < 1$ holds for the internal variable, i.e. microcracks have initiated, however, they have not grown sufficiently large to effect local rupture. The red areas indicate macroscopic cracks as in the previous figures. Maximum temperatures are predicted to be as large as almost 3000 °C, whereas measurements yield maximum values below 2000 °C. An overestimation of temperatures in the simulation is expected due to the adiabatic boundary conditions and an ideal assumption

of heat transfer in the impact zone. The results in Fig. 10, however, are not intended to provide quantitative predictions, without any doubt requiring a more sophisticated modeling of thermal boundary conditions and heat transfer.

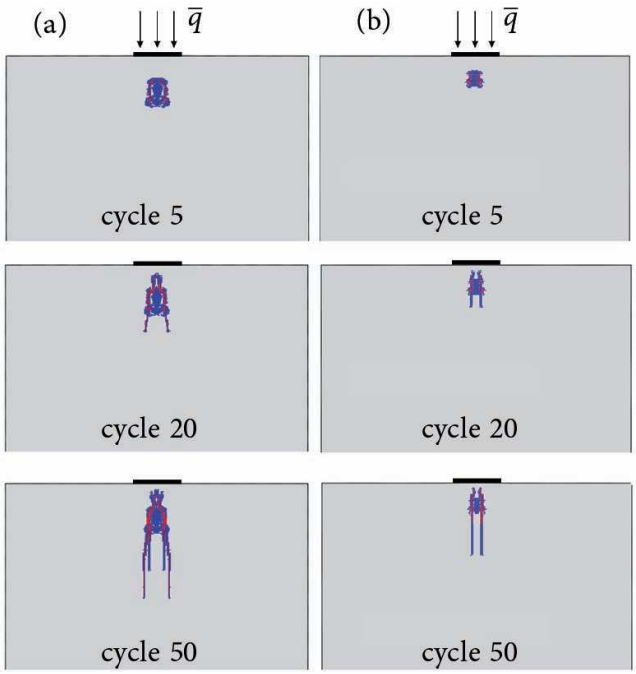

Fig. 10: Simulation of cyclic thermal shocks applied to the surface of a specimen in accordance with experiments [27].

Anyhow, in the experiments damage is not observed at the surface of the specimen, unless a sufficiently large number of cycles has been imposed. The simulations reveal that damage is nucleated underneath the surface at an early stage, approaching the heating zone with increasing number of cycles. Breaking the experimental specimen in two parts after a few load cycles supports this conclusion. In the experiment, however, a damaged surface was observed with fewer cycles than in the simulation, which is attributed to the erosive nature of the electron beam.

The model in Fig. 11 shows the typical shape of a refractory brick with a concavely curved top edge, exposed to a thermal shock heat flux $\bar{q} = 30$ MW/m. Width and height of the model have been chosen as 100 × 80 mm, the bottom edge is mechanically supported allowing for unconstrained extension, and the three edges, not being exposed to the heat flux, are adiabatic. Simulations for three thermal load cycles, as depicted in the plot, are presented in Fig. 11, each one with a heat flux kept constant for 30 seconds, interspersed with 10 seconds of rest. The damage zones or cracks, outlined in red, are shown at the ends of the heating periods. A network of cracks develops, again nucleating underneath the surface and growing with increasing number of thermal shocks. The largest effect on the damage is observed for the first two shocks, while the crack pattern develops moderately with further load cycles.

While the results introduced above show crack patterns, providing an illustrative insight into the extent of damage due to different loading scenarios, Fig. 12 is intended to demonstrate the potential of the simulation tool to assess a refractory material or structure quantitatively with regard to thermal shock resistance or residual strength. A Hasselman diagram [28] has been predicted by numerical simulation based on two different values of the thermal expansion coefficient. One holds the value of the above-discussed results, the other is reduced by 25 %. The plots indicate the critical bending stress σ_B from a three-point bending test of a rectangular bar specimen in terms of the maximum normal stress determined from a handbook formula in connection with the critical fracture load. The values σ_B are plotted versus the quenching temperature, which has been varied in different simulations. In the experiment, just as in the numerical simulation, the specimen is first exposed to a thermal shock, subsequently to three-point bending. Specimens with damage patterns right after the thermal shock are depicted on the right-hand side for two temperature jumps $\Delta\theta$ imposed on the bottom edges.

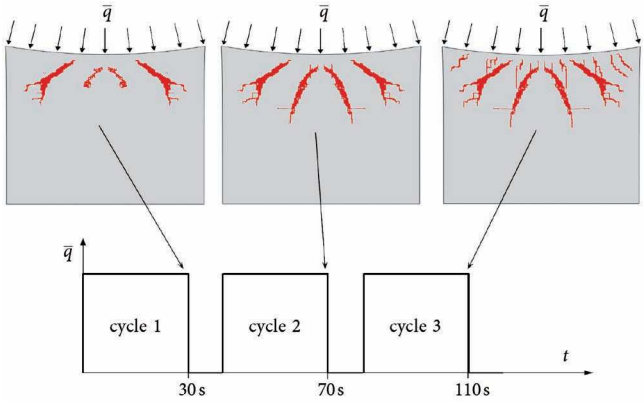

Fig. 11: Thermal shock cycles imposed on a structure resembling a concavely curved refractory brick.

The simulations reveal that the residual strength after the thermal shock is considerably reduced if the quenching temperature exceeds a threshold value $\Delta\theta_{crit}$, the latter amongst other parameters depending on the thermal expansion coefficient α. The damage patterns correspond to the blue curve with the original value $\alpha = 100\,\%$, where $\Delta\theta = 250$ K is below the critical temperature difference, while $\Delta\theta = 380$ K is above. The rigorous drop of residual strength due to thermal shock, allowing for the introduction of $\Delta\theta_{crit}$, is also observed experimentally [29]. Hasselman introduced a thermal shock coefficient $R = \sigma_B(1-\nu)/\alpha E$ to assess the resistance of a refractory material to thermal shock loading. The values for the numerical tests are $R = 608$ K for $\alpha = 100\,\%$ ($\Delta\theta_{crit} = 320$ K) and $R = 1081$ K for $\alpha = 75\,\%$ ($\Delta\theta_{crit} = 490$ K), respectively, where σ_B is inserted from the upper plateau, i.e. for $\Delta\theta \to 0$. The coefficient R allows for qualitative assessments, where large values are desirable. Quantitative predictions require numerical simulations as presented.

In Fig. 13, a graded structure consisting of three ceramic layers is shown. Two different materials have been used, both for experiments that have been performed within the framework of the joint research program and the simulations. In the left figure, the middle layer consists of A21, surrounded by two layers of A1518, in the right figure

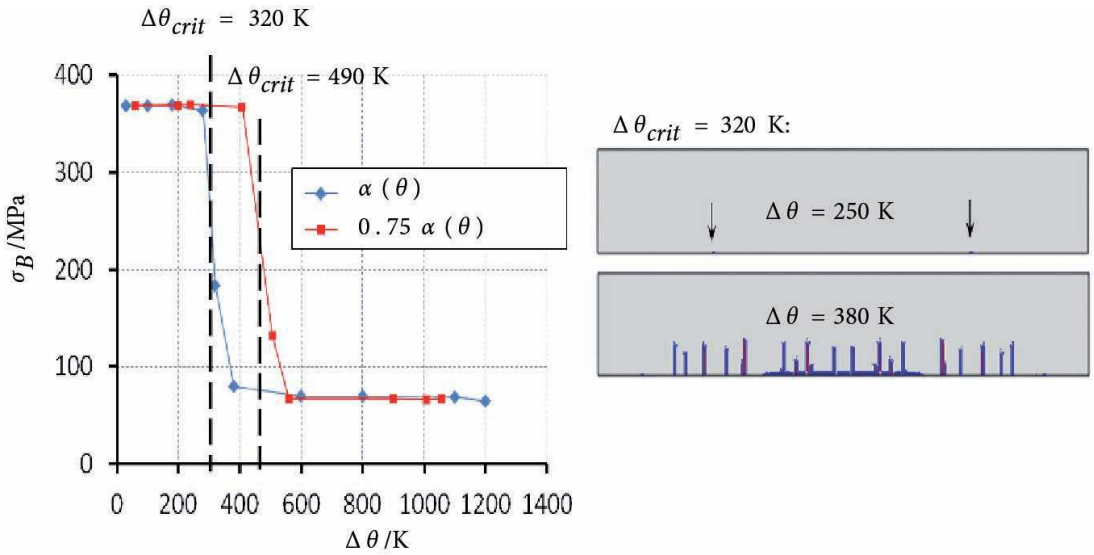

Fig. 12: Hasselman diagram from simulations with different thermal expansion coefficients and thresholds $\Delta\theta_{crit}$ for degradation of residual strength σ_B (left); damaged specimen for $\Delta\theta_{crit}$=320 K corresponding to different quenching temperatures (right).

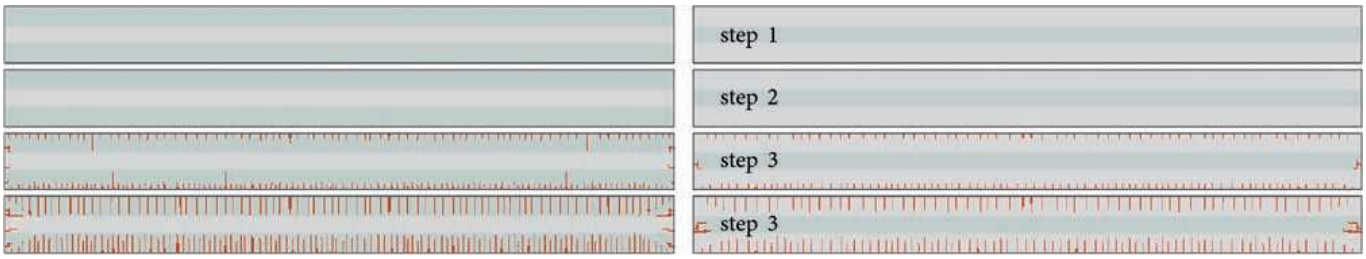

Fig. 13: Simulation of cyclic heating and quenching processes by means of two multilayer systems A1585-A21-A1585 (left) and A21-A1585-A21 (right).

the composition is reversed. Both systems have been exposed to quenching from all sides caused by emerging of the specimens into water after they had been in an oven to a temperature of 1000 °C. Step 1 depicts the condition of the specimen after the linear heating period lasting for 327 minutes. Step 2 shows the state after 30 minutes of constant surface temperature. Step 3 shows results right after the shock cooling to room temperature, which is supposed to take 10 seconds in the simulations. Step 4 displays the condition after further 15 minutes of exposure to room temperature.

Before the specimen is exposed to the above procedure, it has been sintered. Owing to the different shrinkage rates of the two materials, residual stresses are obtained which are compressive in the layers of A21 and tensile in the layers consisting of A1585. In the simulation, this manufacturing process is modeled by assuming suitable thermal extension coefficients in connection with hypothetical, homogeneously distributed temperature changes. The magnitudes of residual stresses in the experiment and in the simulation thus are comparable, amounting to approx. ±60 MPa. In a comparison of the two compositions in Fig. 13, the left one exhibits tensile residual stress in the outer layers, while compressive stress is stored in the surrounding layers of the right one. Besides that, the elastic modulus and specific heat capacity of A1585 are larger than for A21.

Owing to these features it is obvious that the left composition (A1585-A21-A1585) is damaged severely compared to the right one (A21-A1585-A21). In both systems an onset of damage is not observed during the heating period but due to the quenching (step 3). The damage process, however, is not stopped right after reaching room temperature at the surface of the specimen, but continues during further exposure to the environment (step 4). The effect of damage reduction due to compressive residual stress might be smaller than expected, though. In this context, the tensile stress due to thermal loading appears to be about one order of magnitude larger than the compression.

In Fig. 14 the geometry and boundary conditions are the same as in Fig. 11, including an identical thermal loading scheme and results taken at the same instants in time. The simulations, however, are based on the numerical cell model accounting for grain boundaries and intercrystalline crack growth. The parameters for the cohesive laws in normal and shear direction have been chosen as $G_c = 38$ N/m, $\delta^c_{(i)} = 0.5$ µm, $K_{nn} = 3.05 \cdot 1010$ N/mm^3, and $K_{ss} = K_{nn} \cdot 10^{-3}$. A comparison of Figs. 11 and 14 reveals that the damage patterns are similar, indicating four to six isolated branches which could be interpreted as macroscopic cracks or crack networks. All of them tend to di-

verge from the axis of symmetry, both with analytical and numerical cell models. The relative areas of damaged zones are slightly larger for the polycrystalline two-scale FE approach than for the analytical crack model. If the average grain size is reduced from 10 μm to 5 μm, the damage patterns in Fig. 15 are obtained. A size effect is incorporated relating the separation δ to the average grain size, thus $\delta^c_{(i)} = 0.25$ μm and $K_{nn} = 1.21 \cdot 10^{11}$ N/mm³. In contrast to the coarse-grained material according to Fig. 14, the crack network exhibits a much larger density. It is concluded that the thermal shock resistance appears to be negatively affected by the reduction of the grain size, unless the model neglects essential physical or chemical features related to the dimensions of crystallites.

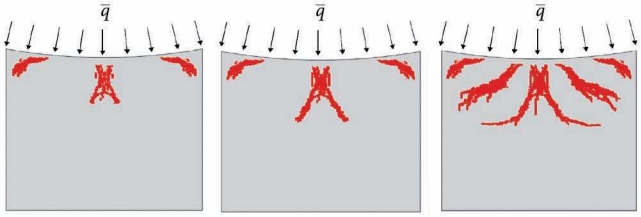

Fig. 14: Periodical thermal shocks on a refractory brick with the identical load history, initial and boundary conditions from Fig. 11 using the numerical cell model of intercrystalline microcrack growth.

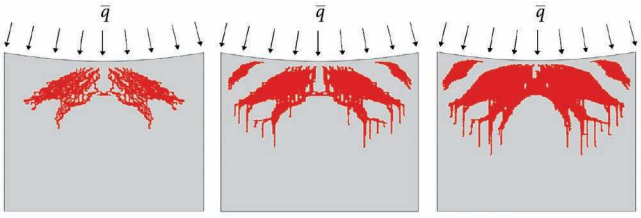

Fig. 15: Refractory brick under thermal shock with decreased grain size, but otherwise the same conditions as in Fig. 14.

IV. Summary

Finite element simulations of mechanically and thermally loaded plane specimens are presented, referring to typical scenarios refractory ceramics are exposed to. It is shown that continuum damage mechanics of brittle solids is capable of predicting paths of macroscopic cracks, although the more appropriate approach in that case certainly remains classical fracture mechanics. Both two-scale models, one on the microscale based on an analytical, the other one on a numerical cell model, have been proven to efficiently predict damage patterns in an illustrative way and to provide quantitative data like threshold temperatures for drastic degradation of residual strength or critical numbers of load cycles. Damage mostly is initiated underneath the surface, remaining invisible for the first few load cycles. The largest part of the damage is attributed to the first thermal shock in a sequence of several cycles. A graded structure in terms of a suitable combination of ceramic layers may improve the thermal shock resistance of a refractory surface coating.

Acknowledgment

Financial support by the German Science Foundation (DFG) within the SPP 1418 program, and by Hessen's State Ministry of Higher Education, Research and the Arts within the LOEWE project "Safer Materials" is gratefully acknowledged.

References

1 Lube, T., Baierl, R.G.: Sub-critical crack growth in alumina – a comparison of different measurement and evaluation methods, *Berg- und Hüttenmännische Monatshefte*, **156**, 450–456, (2011).

2 Supancic, P.H., Schöpf, H.M.: Exact implementation of subcritical crack growth into a weibullian strength distribution under constant stress rate conditions, *J.Eur.Ceram.Soc.*, **32**, 4031–4040, (2012).

3 Henneberg, D., Ricoeur, A., Judt, P.: Multiscale modeling for the simulation of damage processes at refractory materials under thermal shock, *Comput. Mater. Sci.*, **70**, 187–195, (2013).

4 Henneberg, D., Ricoeur, A.: Numerical two-scale simulations of damage evolution at refractory materials, *J. Ceram. Sci. Tech.*, **5**, [2], 83–93, (2014).

5 Kolari, K.: Damage mechanics model for brittle failure of transversely isotropic solids. VTT Technical Research Centre of Finland, 2007.

6 Lemaitre, J., Desmorat, R.: Engineering damage mechanics. Springer-Verlag, Berlin Heidelberg, 2005.

7 Ricoeur, A., Kuna, M.: The thermoelectromechanical J-integral and the thermal permeability of cracks, *Key Eng. Mater.*, **385–387**, 569–572, (2008).

8 Gross, D., Seelig, T.: Fracture mechanics. Springer-Verlag, Berlin Heidelberg, 2011.

9 Nemat-Nasser, S., Hori, M.: Micromechanics: Overall properties of heterogeneous materials. 2nd edition. Elsevier, Amsterdam, 1999.

10 Kuna, M.: Numerical stress analysis of cracks, in German, Vieweg+Teubner, Wiesbaden, 2008.

11 Hill, R.: Elastic properties of reinforced solids: Some theoretical principles. *J. Mech. Phys. Solids*, **11**, 357–372, (1963).

12 Kouznetsova, V.G., Geers, M.G.D., Brekelmans, W.A.M.: Advanced constitutive modeling of heterogeneous materials with gradient-enhanced computational homogenization scheme, *Int. J. Numer. Meth. Engng.*, **54**, 1235–1260, (2002).

13 Gitman, I.M.: Representative volumes and multi-scale modeling of quasi-brittle materials, Ph.D-Thesis, Delft University of Technology, Netherlands, 2006.

14 Miehe, C., Koch, A.: Computational micro-to-macro transitions of discretized microstructures undergoing small stress, *Archive Appl. Mech.*, **72**, 300–317, (2002).

15 Loehnert, S., Belytschko, T.: A multiscale projection method for macro/microcrack simulations, *Int. J. Numer. Meth. Engng*, **71**, 1466–1482, (2007).

16 Oezdemir, I., Brekelmans, M.,G.,D., Geers, M.: FE2 computational homogenization for the thermo-mechanical analysis of heterogeneous solids, *Comp. Methods Appl. Mech. Engrg.*, **198**, 602–613, (2008).

17 Geers, M.G.D., Kouznetsova, V.G., Brekelmans, W.A.M.: Multi-scale computational homogenization: trends & challenges, *J. Comp. Appl. Math.*, **234**, [7], 2175–2182, (2010).

18 Wachtman, J.B., Cannon, W.R., Matthewson, M.J.: Mechanical properties of ceramics, 2nd edition. John Wiley & Sons, Inc., New York, 2009.

19 Barenblatt, B.: The formation of equilibrium cracks during brittle fracture, *J. Appl. Math. and Mech.*, **23**, 622–636, (1959).

20 Dugdale, D.S.: Yielding of steel sheets containing slits, *J. Mech. Phys. Solids*, **8**, 100–104, (1960).

[21] Needleman, A.: A continuum model for voids nucleation by inclusion debonding, *J. Appl. Mech.*, **54**, 525 – 531, (1987).

[22] Hillerborg, A., Modeer, M., Petersson, P.E.: Analysis of crack formation and crack growth in concentrate by means of fracture mechanics and finite elements, *Cement Concrete Res.*, **6**, 773 – 782, (1976).

[23] Rice, J.R.: A path independent integral and the approximate analysis of strain concentration by notches and cracks, *J. Appl. Mech.*, **35**, 379 – 386, (1968).

[24] Griffith, A.A.: The phenomena of rupture and flow in solids, *Phil. Trans. Roy. Soc.*, 163 – 197, (1920).

[25] Judt, P. O., Ricoeur, A., Linek, G.: Crack path prediction in rolled aluminum plates with fracture toughness orthotropy and experimental validation, *Eng. Fract. Mech.*, **138**, 33 – 48, (2015).

[26] Pilipenko, D., Natanzon, Y., Emmerich, H.: Multiscale modeling of thermoshock in aluminium oxide ceramics, *Refractories Worldforum*, **4**, [1], 169 – 174, (2012).

[27] Thomser, C., Skiera, E., Buerger, A., Linke, J., Loewenhoff, T., Schmidt, A., Singheiser, L., Steinbrech, R.: Thermal shock testing of refractory materials using an electron beam materials test facility, *Int. J. Appl. Ceram. Tec.*, **9**, [6], 1098 – 1103, (2012).

[28] Hasselman, D. P. H.: Thermal stress resistance parameters for brittle refractory ceramics. *J. Am. Ceram. Soc.*, **49**, [12], 1033 – 1037, (1970).

[29] Homeny, J., Bradt, R.C.: Thermal shock of refractories. In: Thermal stresses in severe environments. Plenum Press, New York, 1980.